

ARTICLE

Received 13 Feb 2012 | Accepted 23 Apr 2012 | Published 6 Jun 2012

DOI: 10.1038/ncomms1860

Digital quantum simulation of the statistical mechanics of a frustrated magnet

Jingfu Zhang^{1,2,*}, Man-Hong Yung^{3,*}, Raymond Laflamme^{1,2,4}, Alán Aspuru-Guzik³ & Jonathan Baugh^{1,2,5}

Many problems of interest in physics, chemistry and computer science are equivalent to problems defined on systems of interacting spins. However, most such problems require computational resources that are out of reach with classical computers. A promising solution to overcome this challenge is quantum simulation. Several ‘analogue’ quantum simulations of interacting spin systems have been realized experimentally, where ground states were prepared using adiabatic techniques. Here we report a ‘digital’ quantum simulation of thermal states; a three-spin frustrated magnet was simulated using a nuclear magnetic resonance quantum information processor, and we were able to explore the phase diagram of the system at any simulated temperature and external field. These results help to identify the challenges for performing quantum simulations of physical systems at finite temperatures, and suggest methods that may be useful in simulating thermal open quantum systems.

¹ Institute for Quantum Computing, University of Waterloo, Waterloo, Ontario, Canada N2L 3G1. ² Department of Physics and Astronomy, University of Waterloo, Waterloo, Ontario, Canada N2L 3G1. ³ Department of Chemistry and Chemical Biology, Harvard University, Cambridge, Massachusetts 02138, USA. ⁴ Perimeter Institute for Theoretical Physics, Waterloo, Ontario, Canada N2J 2W9. ⁵ Department of Chemistry, University of Waterloo, Waterloo, Ontario, Canada N2L 3G1. *These authors contributed equally to this work. Correspondence and requests for materials should be addressed to J.B. (email: baugh@uwaterloo.ca).

The most challenging aspect of many-body simulation is that the memory and temporal resources often scale exponentially¹, rendering many problems of interest intractable by all known classical methods². A promising solution is quantum simulation^{3–14}, in which one quantum system acts as a processor to simulate another physical system (quantum or classical). There are two classes of quantum simulation: ‘analog’ simulators are typically engineered to simulate a particular class of Hamiltonians¹⁵ and to find ground states of nontrivial Hamiltonians adiabatically, whereas ‘digital’ simulators rely on universal quantum information processors (QIPs)¹⁶, capable of implementing a universal set of quantum gate operations¹⁷ that can, for instance, efficiently simulate the time evolution of an arbitrary initial state under most physically relevant Hamiltonians¹⁸.

Simulations of interacting spin systems¹⁹ are of particular importance to many applications, such as modelling magnetism²⁰, solving optimization problems²¹, and restoring digital images²². Furthermore, understanding the properties of the spin models also offers insights to computational complexity theory²³. For example, the ground-state problem of the Ising spin model is known to be an NP-complete problem^{23,24}. This implies that if an efficient algorithm for solving the ground state of the Ising model exists, then it can solve all other problems in the class of NP. This matter is related to the question whether P equals NP, and is a major unsolved problem in computer science; it is one of the Millennium problems selected by the Clay Mathematics Institute²⁵.

In a series of recent experiments^{3–7} based on adiabatic methods²⁴, great progress in the quantum simulation of spin systems has been made using several physical implementations. These experiments are limited to studying ground-state properties, and require that the energy gaps along the adiabatic paths are large enough to avoid excitations from the ground states²⁴. In general, the energy gaps cannot be predetermined efficiently²⁶, and the controllability of energy gaps is a subject of controversy²⁷. Therefore, the advantage of adiabatic methods over classical methods is not guaranteed in all cases²⁶.

In this paper, we report experimental results for the digital quantum simulation of thermal states of a classical spin system consisting of three antiferromagnetically coupled Ising spins. The ground state of this system is highly degenerate, leading to frustration. A pseudo external field is included in the simulations as an adjustable parameter in probing the variations of the physical properties of the spin system against the changes in the simulated temperature. The experimental implementation was performed using a seven qubit nuclear magnetic resonance (NMR) quantum information processor, where four of the nuclear spins were employed for the simulation. We focussed on simulating the total magnetization and the entropy of the Ising spin system. In both cases, the experimental results agree qualitatively with theoretical predictions, and quantitative deviations from theory are analysed with respect to several error sources. A simple decoherence model is found to account for a large portion of the error.

Results

Digital quantum simulation of thermal states. At finite temperatures, all the equilibrium thermodynamic properties of spin systems can be obtained by determining the partition function \mathcal{Z} , which falls into the complexity class sharp-P, or #P (ref. 28) rather than NP. However, if an efficient algorithm for evaluating partition functions exists, then the ground-state properties of the corresponding spin systems can also be determined efficiently. Therefore, the problem of determining partition functions is at least as hard as the NP-problems, that is, it is NP-hard²⁸.

In practice, partition functions cannot be computed efficiently, except for some simple cases such as 1D spin chains²⁰. For classical spins, the classical Metropolis algorithm²⁹ provide a means

for generating the Gibbs probability distributions²⁰, through the construction of Markov chains with Monte Carlo methods³⁰. For quantum systems, the quantum generalization of the Metropolis algorithm has been found^{31,32}. However, Markov chain-based methods, similar to the adiabatic methods, are limited to the cases where the Markov-matrix gaps cannot be too small to achieve convergence³³. Particularly, for frustrated spin systems¹⁹, Metropolis sampling can result in ensembles trapped in local minima. In these cases, methods for direct encoding of the Gibbs distribution into the states of the qubits would be more efficient^{34,35}. This is the key issue that motivates this experimental work.

Using a digital quantum simulator, the experiments we present are able to explore the full phase diagram of the system’s thermal states as a function of temperature and magnetic field. Well-developed NMR techniques for quantum information processing^{36,37} provide convenient experimental methods to implement a universal set of single-qubit and multiple-qubit gates for building quantum circuits.

Coherent encoding of thermal states. Here we report a digital quantum simulation of the finite-temperature properties of a three-spin frustrated Ising magnet (Fig. 1), using a four-qubit QIP based on NMR. The frustrated magnet exhibits a rich phase diagram of the total magnetization as a function of temperature and magnetic field, and we experimentally probe various distinct features of the system. The phenomenon of geometric frustration^{38,39} is an interesting topic in condensed matter physics⁴⁰. For example, materials such as water ice that exhibit geometric frustration cannot be completely frozen, which renders the entropy finite at zero temperature. Recently, the same three-spin magnet at zero temperature was simulated by trapped ions^{5,6}. Our work extends quantum simulation of this system to finite temperatures, using methods that may be generalized for simulating quantum systems in contact with a thermal environment.

The algorithm implemented here prepares a coherent encoding of a thermal state (CETS) on a quantum register^{34,35},

$$|\Psi_{\beta}\rangle = \sum_k \sqrt{e^{-\beta E_k} / \mathcal{Z}} |\phi_k\rangle, \quad (1)$$

which is a pure state (a pseudo-pure state⁴¹ in the NMR experiment) with amplitudes $\sqrt{e^{-\beta E_k} / \mathcal{Z}}$ equal to the square roots of the corresponding thermal Gibbs probabilities associated with the eigenstate $|\phi_k\rangle$ of Hamiltonian H . Here $\beta = 1/T$ ($k_B = 1$), and $\mathcal{Z} = \text{Tr}(e^{-\beta H})$ is the partition function. The CETS, therefore, contains the same information as the thermal density matrix

$$\rho_{\text{th}} = e^{-\beta H} / \mathcal{Z} \quad (2)$$

of the simulated system. ρ_{th} can be directly obtained from the CETS state $|\Psi_{\beta}\rangle$ by artificially ‘decohering’ the off-diagonal elements of the CETS density matrix $|\Psi_{\beta}\rangle\langle\Psi_{\beta}|$ (ref. 35). In our implementation, we measure the diagonal elements of the CETS density matrix and do not engineer decoherence.

The number of quantum gates needed for this method³⁵ of preparing the CETS is linear in the number of spins for one-dimensional systems and sub-exponential in two dimensions, but is exponential for the general cases that correspond to NP-problems. Nonetheless, the efficiency of the algorithm is independent of the simulated temperature and not limited by the small-gap problem encountered in the Markov-Chain Monte Carlo algorithms. This provides an advantage for simulating the low-temperature properties of frustrated spin systems. Furthermore, although these algorithms can at most yield a quadratic speedup for simulating the

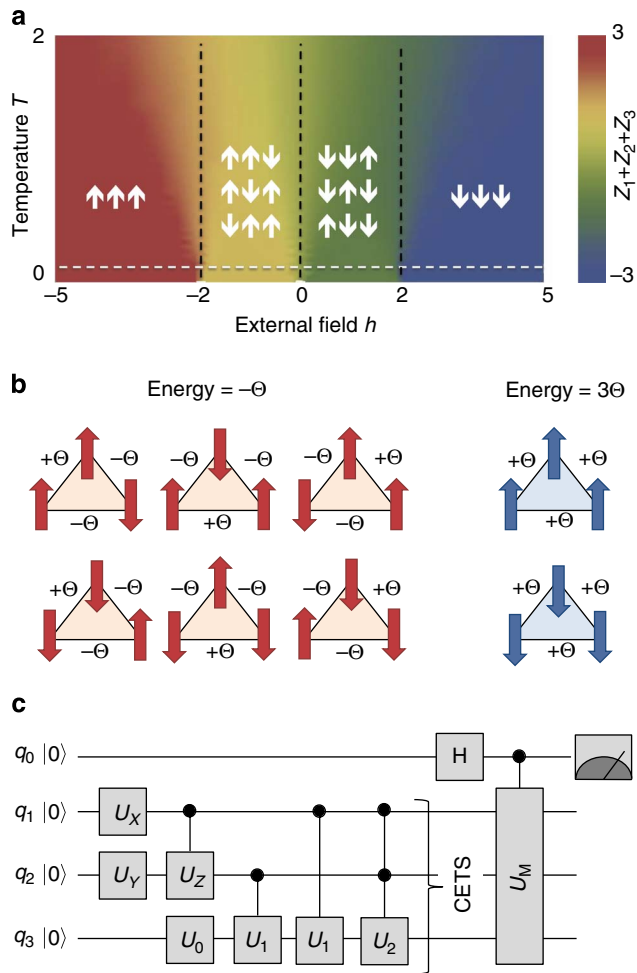


Figure 1 | Theoretical description of the frustrated magnet. (a) Theoretical phase diagram of the magnetization. The units of the axes are k_B and Θ for temperature and external field, respectively. The white dashed line parallel to the h -axis denotes $T = 1/\beta = 1/11$, which corresponds to the experimental data shown in Fig. 3. (b) All possible configurations of a three-spin frustrated Ising magnet at zero temperature and zero magnetic field. The ground state is sixfold degenerate, leading to a non-zero entropy. (c) Quantum circuit diagram for preparing and measuring the CETS $|\Psi_\beta\rangle$ defined in equation (1) from the initial state $|0000\rangle$. The unitary gates are $U_x = R(\theta_x)$, $U_y = R(\theta_y)$, $U_z = R(\theta_z - \theta_y)$, $U_0 = R(\theta_0)$, $U_1 = R(\theta_1 - \theta_0)$ and $U_2 = R(\theta_2 - 2\theta_1 + \theta_0)$, where $R(\theta) = e^{-i\theta Y}$ and Y denotes the y -component of the Pauli matrices. The explicit expressions for the angles as functions of β , h and Θ are given in the Supplementary Methods. The upper qubit q_0 serves as a probe for measuring the physical observables. H indicates a Hadamard gate, and U_M is the operator corresponding to the observable being measured.

most general thermal states³⁵, the subclass of the CETS which can be created efficiently on a quantum computer can serve as a ‘heat bath’⁴² and may yield an exponential speedup over classical methods when simulating the dynamics of open quantum systems⁴³. Our goal is to demonstrate that the CETS for a system showing geometric frustration can be prepared in the laboratory precisely enough to extract useful thermodynamic information.

Simulation of a frustrated magnet subject to an external field.

In this experiment, three qubits encode the CETS of a triangle plaquette of Ising spins with equal couplings Θ , at temperature T and subject to a global magnetic field h . A fourth ancilla qubit is

used to probe the physical properties of the CETS by measuring the set of diagonal Pauli operators, so that the spin magnetizations and correlations can be extracted. These measurements are sufficient to determine the partition function Z , from which any thermodynamic quantity of interest, such as entropy S , can be calculated.

The Hamiltonian of the frustrated magnet subject to an external field is given by^{19,39}

$$H = \Theta(Z_1 Z_2 + Z_2 Z_3 + Z_1 Z_3) + h(Z_1 + Z_2 + Z_3), \quad (3)$$

where $Z_i \equiv \sigma_i^z$ is the \hat{z} Pauli matrix of the spin i . For $\Theta > 0$, the coupling is antiferromagnetic, and the spins tend to minimize energy by pointing in opposite directions. The external field h , however, tends to force the spins to align. A finite temperature T serves to mix up these tendencies. These competing factors give rise to a rich phase diagram shown in Fig. 1a. For example, at low temperature and near some critical values of the external field $h = -2\Theta$, 0 and 2Θ (we set $\Theta = 1$ in the following), there are crossover points where the spin configuration, and hence the total magnetization, changes abruptly. Near $h = 0$, the ground state is fully frustrated with a six-fold degeneracy, as illustrated in Fig. 1b. This means that, unlike ordinary materials, the entropy and heat capacity of the spin system remain finite as $T \rightarrow 0$.

For any given value of temperature and magnetic field, the CETS $|\Psi_\beta\rangle$ can be prepared with a quantum circuit of constant size, as shown in Fig. 1c. The three lower qubits, q_1 , q_2 and q_3 , initialized into the $|000\rangle$ state, are the register qubits used to encode the CETS. We use the phase kick-back method for readout¹⁷ by introducing a fourth ‘probe’ qubit q_0 , exploiting the fact that all spin–spin (J) couplings are well resolved for this qubit (see Methods section). All information contained in the CETS is gained by measurements on the probe qubit, so that we avoid experimental difficulties with direct readout of qubits $q_1 - q_3$ owing to poor spectral resolution of certain spin–spin couplings. We did, however, implement direct state tomography of the register qubits for certain states to compare readout methods and to quantify errors (see Discussion and Methods), but we found this to be generally unreliable for arbitrary states. All elements of an arbitrary density matrix can be reconstructed using the phase kick-back method, if the density matrix is expanded in the product operator basis⁴⁴.

The probe is shown as the upper qubit in Fig. 1c and is prepared in a superposition state $(|0\rangle + |1\rangle)/\sqrt{2}$ just prior to readout. A controlled- U_M gate is then applied to the joint probe-CETS system to measure observables $\langle U_M \rangle = \langle \Psi_\beta | U_M | \Psi_\beta \rangle$. Here $\langle U_M \rangle$ is proportional to the coherent part of the reduced density matrix of the probe qubit obtained by tracing over qubits $q_1 - q_3$:

$$\rho_0 = \frac{1}{2} \begin{pmatrix} 1 & \langle U_M \rangle \\ \langle U_M \rangle^* & 1 \end{pmatrix} \quad (4)$$

$\langle U_M \rangle$ is extracted from the NMR signal of the probe qubit after application of the controlled- U_M gate. A Hamiltonian of the classical Ising type (i.e. equation (3)) leads to a purely diagonal thermal state density matrix. Hence, by measuring the set of observables that span the diagonal matrix elements,

$$U_M = \{Z_1, Z_2, Z_3, Z_1 Z_2, Z_2 Z_3, Z_1 Z_3, Z_1 Z_2 Z_3\}, \quad (5)$$

the thermal state density matrix ρ_{th} can be reconstructed (see equation (6) below).

Experimental results for magnetization and entropy. In the experiment, we use the four carbon spins of ¹³C-labelled trans-crotonic

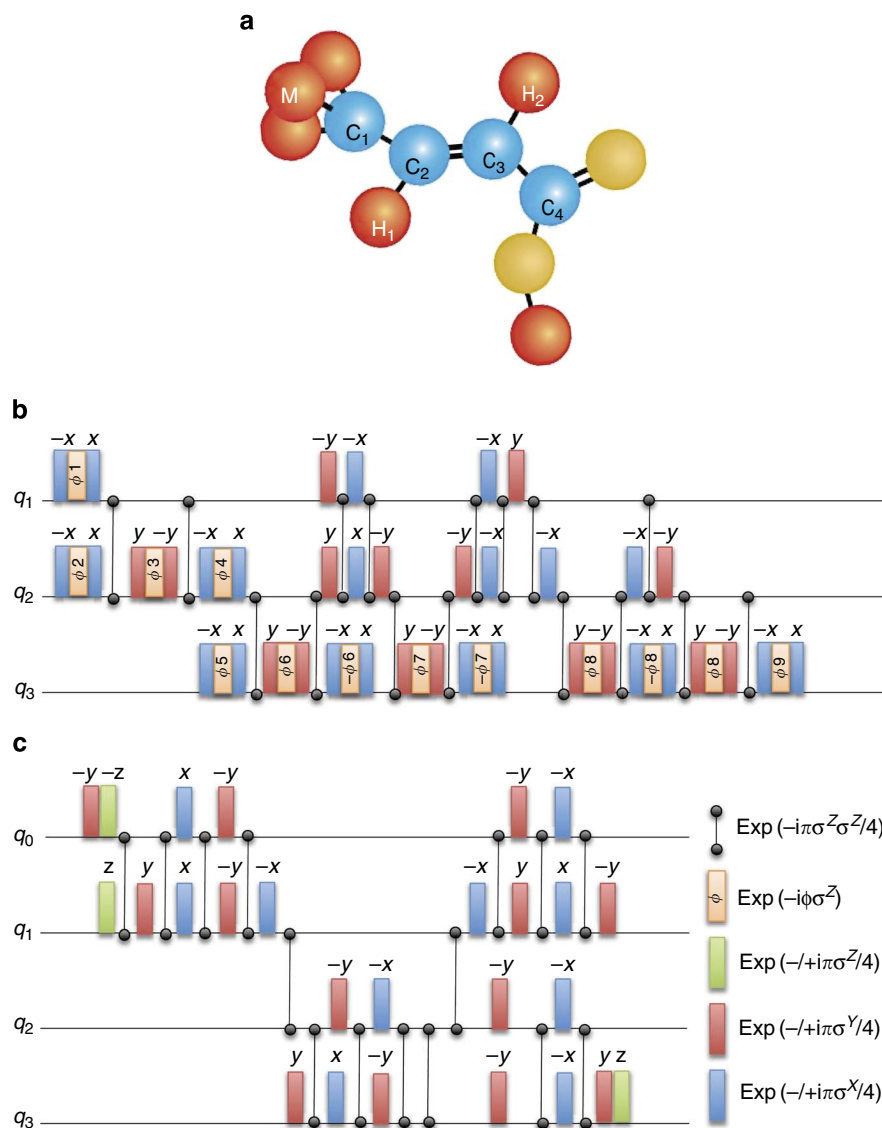


Figure 2 | Experimental protocol. (a) The molecular structure of carbon-13-labelled trans-crotonic acid. C₁–C₄ label ¹³C spins, and M, H₁ and H₂ label protons. (b,c) Pulse sequences for (b) preparing the CETS on qubits q₁–q₃, and (c) measuring observable Z₁Z₂Z₃ via the top 'probe' qubit q₁ (refocussing pulses are omitted in both circuits for clarity). The three carbons C₂–C₄ are the CETS register qubits q₁–q₃, and C₁ serves as the probe qubit. The RF phase shifts are determined by $\phi_1 = \theta_x$, $\phi_2 = \theta_y - \frac{\pi}{4}$, $\phi_3 = (\theta_z - \theta_y)/2$, $\phi_4 = -(\phi_3 + \frac{\pi}{4})$, $\phi_5 = \theta_0 - \frac{\pi}{4}$, $\phi_6 = (\theta_1 - \theta_0)/2$, $\phi_7 = -(\theta_2 - \theta_0)/4$, $\phi_8 = -(\theta_2 - 2\theta_1 + \theta_0)/4$, $\phi_9 = -\phi_8 + \frac{\pi}{4}$, where the rotation angles θ_k ($k = x, y, z, 0, 1, 2$) are listed in Supplementary Methods.

acid dissolved in d₆-acetone as the four qubit register⁴¹. The structure of the molecule and spin Hamiltonian parameters are shown in Fig. 2a and Table 1, respectively. Using well-known quantum gate decompositions^{45,46}, we first decomposed the controlled-unitary operations in Fig. 1b,c into single-qubit rotations and controlled-NOT gates (Supplementary Fig. S1), where the elementary gates can be implemented using a combination of radio-frequency (RF) pulses and evolutions under the spin–spin J-couplings (for example, see refs 36,37). The NMR pulse sequences were further simplified to minimize the number of pulses needed, resulting in the pulse sequence shown in Fig. 2b for preparing the CETS, and the sequence shown in Fig. 2c for measuring $\langle U_M \rangle = \langle Z_1 Z_2 Z_3 \rangle$, for example. In the CETS preparation sequence, RF phase shifts are exploited to implement the variable angle \hat{z} -rotations ϕ_k from which we construct the variable angle qubit rotations required by the algorithm. Hence, the pulse sequences for every (h, T) point are identical up to RF phase shifts; the phase shifts are implemented with high

precision in NMR (resolution $\sim 10^4$ per rad), and require no evolution time.

The experimental results are summarized as follows: the diagonal elements of the density matrix corresponding to the CETS are determined by measuring the set of diagonal Pauli operators (equation (5)) for a range of simulated temperatures and external fields. Figure 3 shows example NMR spectra of the probe qubit (C₁). Figure 3a shows the NMR spectra of C₁ obtained by a $\pi/2$ readout pulse, when the system is in the labelled pseudo-pure state⁴¹ $\rho_s = 00\sigma_z 0000$ (red) and a reference state $\rho_{\text{ref}} = \sigma_z 11\sigma_z 1111$ (blue), respectively, where 1 is the identity matrix, $0 \equiv |0\rangle\langle 0|$, and the order of qubits is given by: M, H₁, H₂, C₁, C₂, C₃, C₄. We employ the deviation density matrix formalism⁴⁷ throughout this work. Figures 3b,c show spectra corresponding to measurements of $\langle Z_1 Z_2 Z_3 \rangle$ in experiment and by simulation, respectively, with $\beta = 5$, $h = -1$ (red), 0 (blue), and 1 (black). In each spectrum, only the spectral peaks corresponding to spin M in the state $|0\rangle$ are shown,

Table 1 | Hamiltonian parameters for the nuclear spins in carbon-13-labelled trans-crotonic acid.

	M	H ₁	H ₂	C ₁	C ₂	C ₃	C ₄
M	−1301						
H ₁	6.88	−4859					
H ₂	−1.72	15.52	−4078				
C ₁	127.16	3.98	6.36	−2996			
C ₂	−7.10	155.42	−0.66	41.62	−25,516		
C ₃	6.58	−1.74	161.00	1.46	69.66	−21,585	
C ₄	−0.94	6.46	3.72	7.02	1.18	72.16	−29,457
T ₂ (s)	0.80	0.76	0.74	1.02	0.92	0.87	0.94
T ₁ (s)	2.4	3.2	3.3	5.7	5.3	5.6	10.2

The chemical shifts and *J*-coupling constants (in Hz) are listed on and below the diagonal, respectively, in the table. The longitudinal and transversal relaxation times *T*₁ and *T*₂ measured by standard inversion recovery and Hahn echo pulse sequences are listed at bottom. The chemical shifts are given with respect to reference frequencies of 700.13 MHz (proton) and 176.05 MHz (carbon). The molecule has seven qubits because the methyl group M can be treated as a single qubit, using a gradient-based subspace selection method⁴¹.

as the peaks corresponding to M in state $|1\rangle$ are negligibly small. For reference, Fig. 3d shows simulated spectra of C₁ corresponding to spin H₂ in state $|0\rangle$ (red) and $|1\rangle$ (blue) with C₂–C₄ in the state $\mathbb{1}^{\otimes 3}$.

Figure 4a shows the results of measuring the total magnetization $Z_1 + Z_2 + Z_3$ over a range of fields $-5 \leq h \leq 5$ at a low temperature, $\beta = 11$. The raw experimental results are in good agreement with a numerical simulation of the NMR experiments that takes into account the decoherence of the nuclear spins during the computation. The magnetization is seen to change in steps as the simulated field is varied, with critical points located at $h = \pm 2$, and 0, in agreement with the phase diagram in Fig. 1a. The data shown in Figs 4a–d labelled as black stars are rescaled based on a simple depolarization channel decoherence model that assumes uniform error rates for all qubits and has no free parameters (see Supplementary Methods). This rescaling partially removes errors due to decoherence of the probe qubit during the readout step, and clearly improves the agreement with theory. A slight asymmetry of the experimental results with respect to the sign of h is evident in Figs 4a–d, and may arise from the spin-lattice (*T*₁) relaxation of the carbon spins, which was not included in the numerical simulations (see Methods).

Spin correlation functions were also probed systematically for a range of the simulated temperatures and external fields. Selected results are shown in Fig. 4e. From this data, the thermal state density matrix may be constructed for any (h, T) point, subject to the normalization condition $\text{Tr}(\rho_{\text{th}}) = 1$:

$$\rho_{\text{th}} = \frac{1}{8} \mathbb{1} + \sum_i a_i Z_i + \sum_{j < k} b_{jk} Z_j Z_k + c Z_1 Z_2 Z_3, \quad (6)$$

where $a_i = \langle Z_i \rangle / 8$, $b_{jk} = \langle Z_j Z_k \rangle / 8$, and $c = \langle Z_1 Z_2 Z_3 \rangle / 8$, and the expectation values here represent only the real-valued parts (the imaginary parts are zero in theory but non-zero in experiment due to errors; see Discussion). With complete knowledge of ρ_{th} , all macroscopic thermodynamic observables can be determined for an ensemble of frustrated magnets. In this study, we are particularly interested in obtaining the entropy,

$$S = -\text{Tr}(\rho_{\text{th}} \ln \rho_{\text{th}}), \quad (7)$$

which acts as a signature of frustration. Because of its nonlinearity, *S* is expected to be more sensitive to experimental errors than quantities that depend linearly on ρ_{th} such as magnetization.

Figure 5a shows the experimental results for *S* as a function of the simulated magnetic field *h* in the low-temperature regime ($\beta = 11$), compared with theory. Sharp changes in *S* are observed near the same critical points seen in the magnetization data. The larger values of *S* in the region $|h| < 2$ compared with the outer

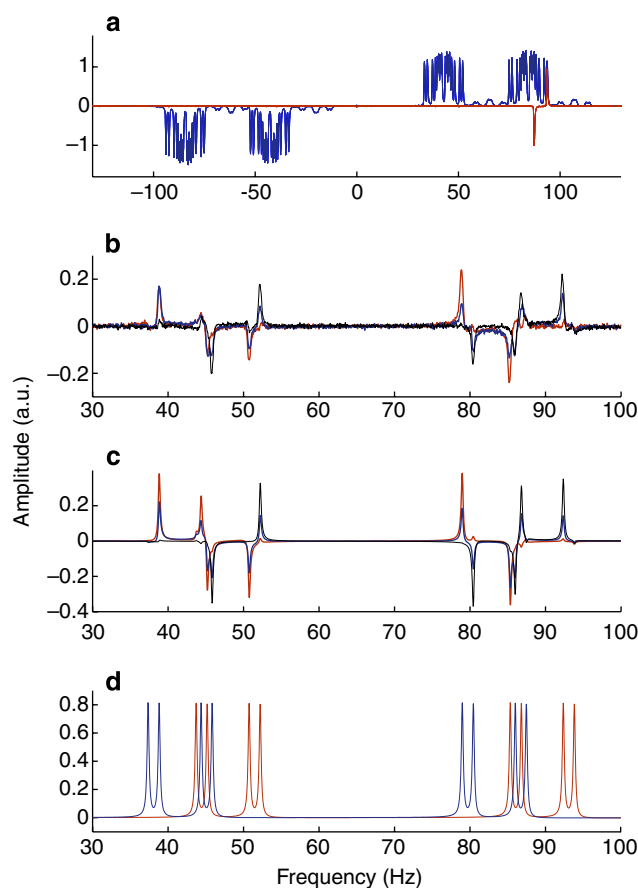


Figure 3 | NMR spectra of the probe qubit C₁. (a) Spectra of C₁ obtained by $\pi/2$ readout pulses when the system is in the labelled pseudo-pure state $\rho_s = \mathbf{00}\sigma_z\mathbf{0000}$ (red) and reference state $\rho_{\text{ref}} = \sigma_z \mathbb{1} \mathbb{1} \sigma_z \mathbb{1} \mathbb{1}$ (blue), respectively, where $\mathbb{1}$ is the identity matrix, $\mathbf{0} \equiv |0\rangle\langle 0|$ and the qubit order is given by MH₁H₂C₁C₂C₃C₄. All vertical axes have the same scaling (arbitrary units). (b,c) Spectra of C₁ for measuring $\langle Z_1 Z_2 Z_3 \rangle$ in experiment (b) and by simulation that includes carbon *T*₂ effects (c), with $\beta = 5$, $h = -1$ (red), 0 (blue), and 1 (black). In each spectrum, only the peaks corresponding to spin M in the state $|0\rangle$ are shown, as the peaks corresponding to M in state $|1\rangle$ are negligibly small. (d) For reference, simulated spectra of C₁ corresponding to spin H₂ in state $|0\rangle$ (red) and $|1\rangle$ (blue) are shown (with C₂–C₄ in the state $\mathbb{1}^{\otimes 3}$).

region $|h| > 2$ indicate the preference of anti-ferromagnetism leading to frustration. A peak at $h = 0$, indicating maximal degeneracy of the ground state, is seen in both the experiment and theory. For the

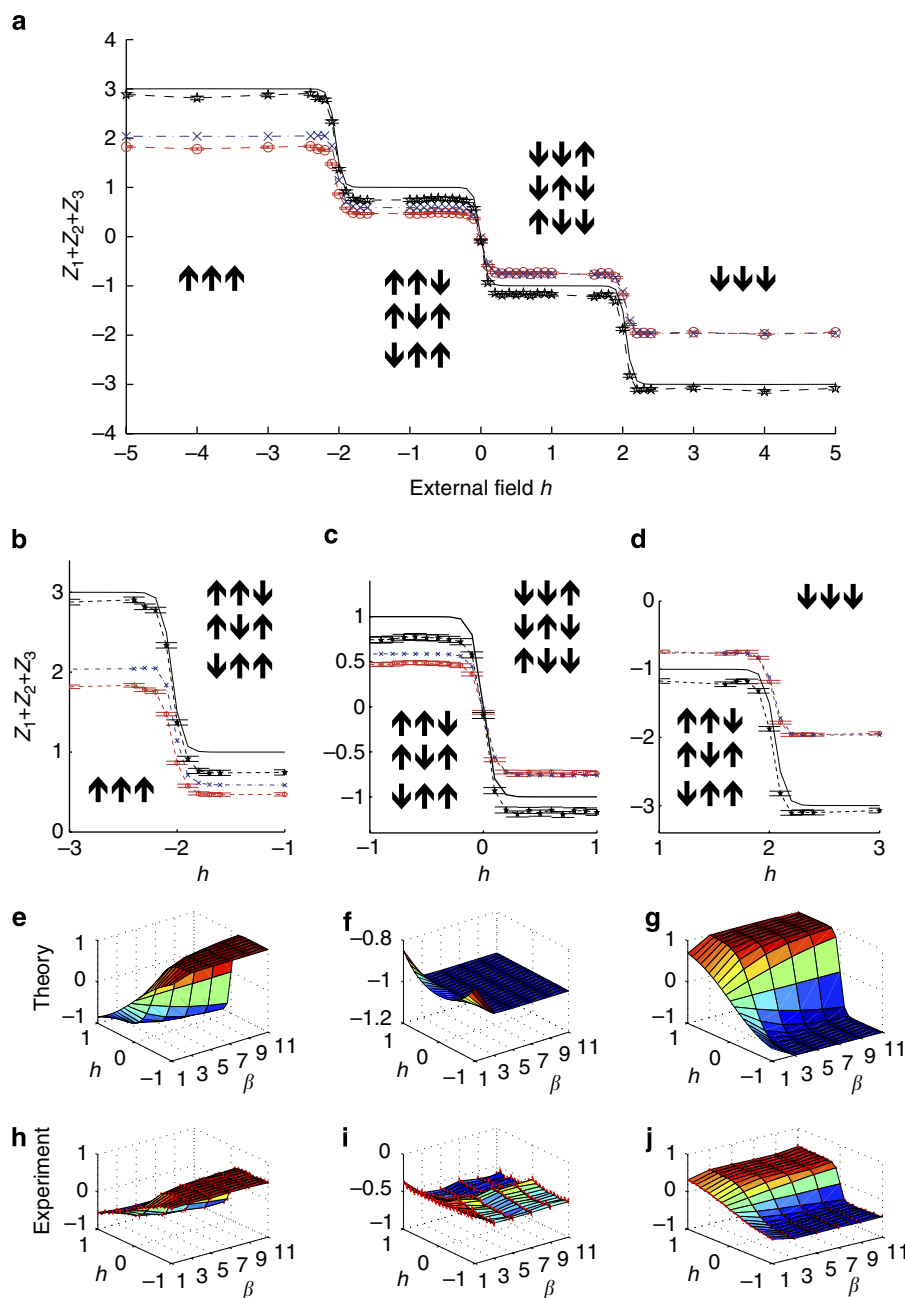


Figure 4 | Experimentally measured magnetization and spin correlations. (a) Total magnetization $Z_1 + Z_2 + Z_3$ as a function of magnetic field h for a low temperature, $\beta = 11$. The theoretical result is shown by the black solid curve. The experimental data (red open circles) is plotted together with numerical simulation results (blue crosses) that include effects of carbon T_2 and proton T_1 . The points labelled by black stars are obtained from the experimental data by the use of a simple decoherence model to partially remove the effects of decoherence (see Supplementary Methods). Error bars are estimated from the uncertainty of the spectral fitting parameters in experimental data analysis. The sharp changes in magnetization show the phase transitions, and the regions around the critical points $h = \pm 2, 0$ are enlarged as figures (b–d). (e–j) Surface plots showing the theoretical values for total magnetization (e) $Z_1 + Z_2 + Z_3$ and spin correlations (f) $Z_1Z_2 + Z_2Z_3 + Z_1Z_3$ and (g) $Z_1Z_2Z_3$, where $1 \leq \beta \leq 11$ and $-1 \leq h \leq 1$. The corresponding experimental values are shown in (h–j), respectively, with experimental uncertainties indicated (error bars in red).

outer region $|h| > 2$, the external field is strong enough to polarize the magnet leading to a theoretical entropy of zero. However, both the raw and rescaled experimental results yield finite values of S . This discrepancy is mainly due to decoherence of the nuclear spin qubits during the computation, as expected from the durations of the pulse sequences (see Discussion, Supplementary Table S1 and Supplementary Fig. S2), and confirmed by numerical simulation

results. The rescaled results are closer to theory, but are still offset significantly, because the actual errors are not uniform across qubits and are not independent of which observable is measured (the readout pulse sequences have different durations). The surface plots in Figs 5b–d show S as a function of h and β in theory (b), simulation (c), raw experimental data (d), and rescaled experimental data (e). The role of increasing temperature is to ‘wash out’

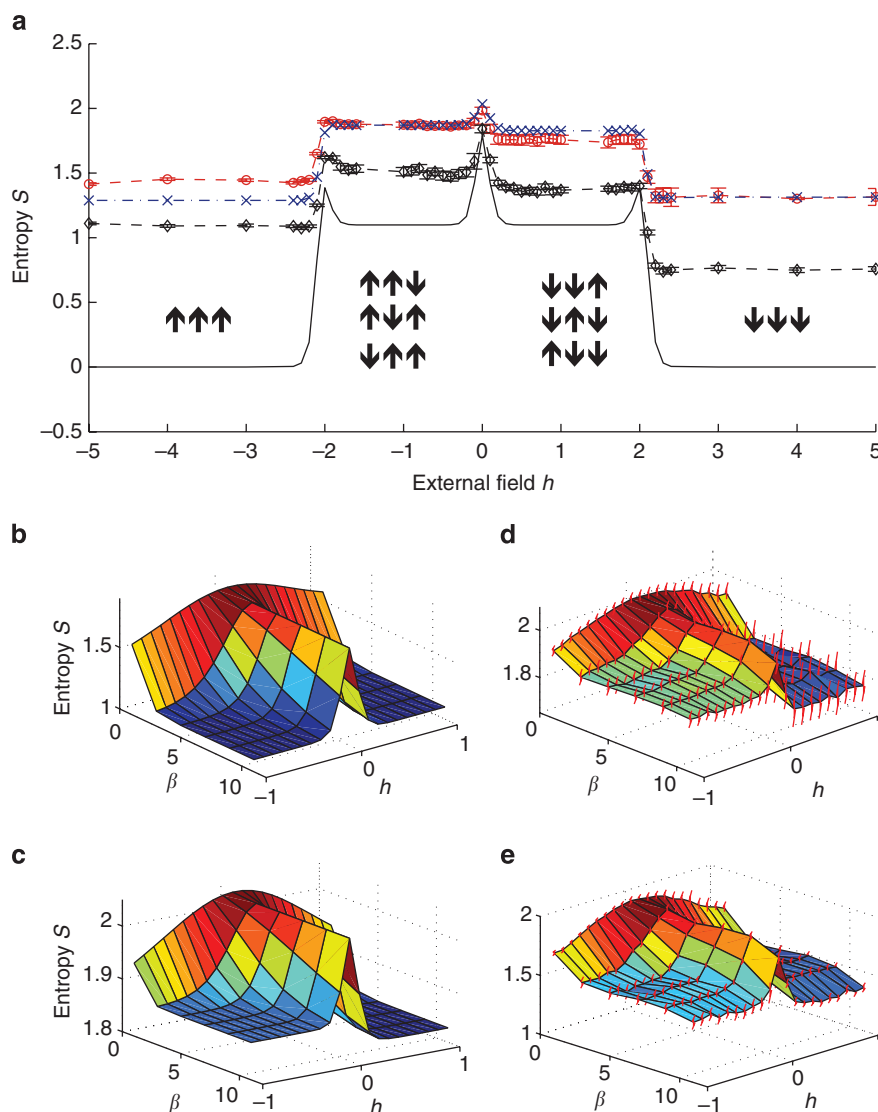


Figure 5 | Entropy of the encoded thermal states. (a) Entropy S as a function of magnetic field h at low temperature, $\beta = 11$. The experimental data (open circles) is plotted together with numerical simulation results (crosses) that include effects of carbon T_2 and proton T_1 . The theoretical result is shown by the solid curve. The sharp changes of S around $h = \pm 2, 0$ indicate the phase transitions. The points labelled by black stars are obtained from the experimental data by the use of a simple decoherence model to partially remove the effects of decoherence. (b–e) Surface plots of entropy as a function of $-1 \leq h \leq 1$ and $1 \leq \beta \leq 11$ in theory (b), numerical simulation (c) and experiment (d). The rescaled experimental results are shown in (e).

the competition between the antiferromagnetic couplings, so that sharp crossovers are not observed in theory or experiment as β is decreased.

Discussion

In the following, we discuss in more detail the sources of error affecting our NMR implementation. For example, consider as a benchmark state the CETS corresponding to $\beta = 11$ and $h = 5$, where the Ising spins are polarized. We numerically simulated the CETS preparation pulse sequence both including and not including the nuclear spin T_2 process, and also measured the experimental density matrix using direct state tomography. The results are summarized in Fig. 6. The error bars on the data measured by direct state tomography of the CETS are much larger than for phase kick-back; this is due to the inability to fully resolve all J -couplings on spins C_2 – C_4 . Figure 6g shows the imaginary elements present in the numerical simulation that does not include T_2 effects. The imaginary elements

on the diagonal are zero in both simulations (g) and (h), but are non-zero in experiment. These elements are due to phase distortions of the readout signals with respect to the reference signal. The average of the root-mean-square of all the imaginary elements on the diagonal, relative to the norm of the real-valued diagonal elements, is 0.077 in experiment and 0.034 in the simulation (not shown) of the full experiment (preparation + readout) that includes T_2 . Hence, the overall magnitude of this error is small, and is in fact related to the output state fidelity in a second order way, because for a small phase error δ the imaginary elements will be proportional to $\sin(\delta) \propto \delta$ whereas the fidelity will be proportional to $\cos(\delta) \propto 1 - \delta^2$. For the real-valued data, note the qualitative correspondence between (c) and (e), the simulation results including T_2 and the phase kick-back results.

Now, we use the state correlation fidelity defined as $\text{Tr}(\rho\rho_0)$ for quantitative analysis, where ρ_0 is the ideal density matrix and ρ is either the result of numerical simulation of the NMR experiment

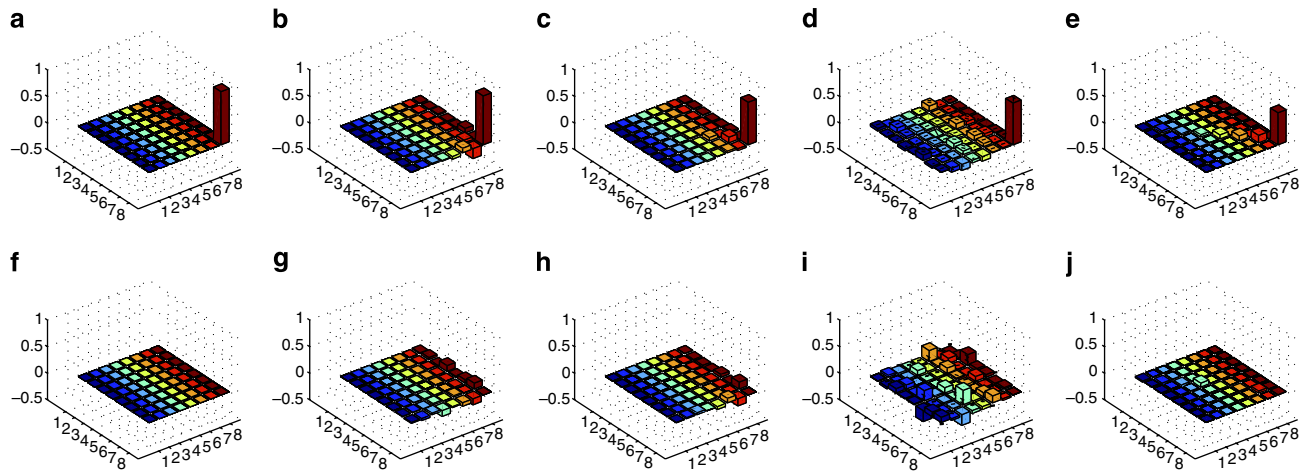


Figure 6 | Density matrices for the coherently encoded thermal state at $\beta=1/T=11$ and $h=5$. (a–e) From left to right, the five columns show the real parts of the density matrices (a) in theory, (b) by simulation without carbon T_2 , (c) by simulation including carbon T_2 , (d) in experiment by full state tomography, and (e) in experiment using the phase kick-back readout. The first three columns show the state just after the CETS preparation. The bottom rows (f–j) show the corresponding imaginary parts of the density matrices. Compared with the theoretical result, the state fidelities from the simulation without T_2 , simulation with T_2 , state tomography and phase kick-back method are 0.919, 0.798, 0.782 ± 0.042 and 0.602 ± 0.002 , respectively. Here we define the fidelity of a measured state ρ as $\text{Tr}(\rho\rho_0)$, where ρ_0 denotes the ideal state. The errors in phase kick-back are estimated from the uncertainty of the fitting parameters and are less than 0.01, so are not shown here. For the full state tomography results shown in (d) and (i) (measured directly using the spectra of C_2 – C_4), the amplitude of each peak is measured by integrating over a range of frequency, because the imperfect resolution of some peaks renders a spectral fit unreliable. The peak integration range is typically 0.40 Hz. The average uncertainty of each measured matrix element is ± 0.035 (d) and ± 0.051 (i), consistent with the greater scatter seen in the data compared to the phase kick-back results. This illustrates the benefit obtained from using C_1 , which has well-resolved spectra, as the probe qubit.

or experimental data. The state correlation obtained from numerical simulation of the CETS preparation without including the T_2 process is 0.92, where the 8% infidelity is due to undesired evolution under J -couplings, finite pulsewidth and off-resonance effects, all of which are minimized by our refocussing scheme but are not removed perfectly. Including T_2 in the simulation reduces the state correlation further to 0.80. The state correlation obtained from experimental state tomography is 0.782 ± 0.042 , from which we can estimate that the errors from experimental pulse imperfections account for at most a few percent of the infidelity. The total number of pulses in the CETS preparation sequence (including refocussing pulses) is 104, suggesting an average error per pulse $\sim \mathcal{O}(10^{-4})$. This relatively low error rate due to non-ideality of pulses is in accord with other recent NMR QIP experiments^{37,48}, and shows that we are able to implement standard qubit-selective pulses and coupling gates with high fidelities. Performing readout on the same CETS using the probe qubit phase kick-back method (for example, Fig. 1c) results in a state correlation of 0.602 ± 0.002 . This is reasonable because of the durations of the additional readout circuits (ranging from 20 to 410 ms) that cause $\langle U_M \rangle$ to decay under T_2 . The aforementioned rescaling procedure, when applied to the density matrix measured via the probe qubit, gives a modified state correlation of 0.881 ± 0.034 . This is consistent with the fidelity we would expect from the experiment with the effects of T_2 removed. The rescaled entropy results plotted in Fig. 5a are roughly consistent with this level of infidelity; for example, if one takes the ideal density matrix at $\beta=11$ and $h=5$ and scales all the observables (a_i , b_{jk} , c in equation (6)) by a factor of 0.88, the corresponding entropy would be 0.54 rather than ~ 0 . However, the observables measured in our experiment are not all scaled by the same factor, because of different durations of the readout sequences and to deviation of the actual error process from the simple uniform-error model. The rescaled experimental entropy, averaged over its values at $h = \pm 5$, is 0.93 ± 0.01 .

It is possible to reduce the duration of the pulse sequences, and thus the effects of decoherence, by using numerically derived optimal control pulses⁴⁹ to implement the circuit unitaries. Recent NMR QIP experiments have illustrated the use of this technique^{50,51}, which allows the unitaries to be implemented in a nearly time-optimal manner. However, these techniques require full classical simulation of the unitary dynamics, rendering straightforward application of the approach impractical for large numbers of qubits. On the other hand, the pulse sequences implemented in this work were derived in a completely scalable fashion³⁷. To achieve high fidelity in larger NMR processors such as are possible in the solid-state^{52,53}, it may be necessary to achieve a hybrid of the two methods that is inherently scalable but uses optimal control on subsystems of fixed qubit number⁵¹.

In summary, our NMR implementation of the CETS preparation and readout uses a scalable quantum gate decomposition and obtains the principal thermodynamic features of the three-spin frustrated Ising magnet. We explored the phase diagram for a range of simulated temperatures and global fields, studying the competition between the antiferromagnetic couplings and the polarizing field. The crossover points were correctly captured in both magnetization and entropy, and the increases in entropy signifying frustration were obtained, including the peak in entropy at low temperature and zero field. The experimental results were found to agree very well with numerical simulations of the NMR experiment. The discrepancies between these results and the ideal theory results are mainly due to the attenuation of expectation values caused by decoherence during the computation, and, to a lesser extent, the imperfect design of the refocussing pulse sequences. Experimental pulse imperfections gave a relatively small contribution to the total error, verifying the high level of control achievable in NMR and suggesting that control is not a fundamental limitation for implementing similar algorithms in larger Hilbert spaces. We believe that techniques used here can be adapted to other physical systems used to

realized QIPs, such as nitrogen vacancy centres in diamond¹⁶. The ability to deterministically prepare a CETS on a subset of qubits in a larger quantum simulation provides a new method, in principle, to simulate contact between a quantum system of interest and a heat bath at arbitrary temperature T . This may provide an economical means for simulating open quantum systems, particularly for thermal states of systems with multifold degenerate ground states.

Methods

NMR implementation. For the NMR implementation, we used ¹³C-labelled trans-crotonic acid dissolved in d6-acetone, which forms a seven-qubit register; the four qubits in this experiment correspond to the four carbon spins, and the three proton spins are not directly involved after the preparation of the pseudo-pure state⁴¹. The experiments were carried out on a 700-MHz NMR spectrometer (Bruker DRX). The structure of the molecule and the Hamiltonian parameters of the seven spin qubits are shown in Fig. 2a, with the spin Hamiltonian given by

$$H_{\text{NMR}} = \pi \sum_j v_j \sigma_j^z + \pi \sum_{k<l} J_{kl} \sigma_k^z \sigma_l^z / 2, \quad (8)$$

where v_j and σ_j^z denote the chemical shift and z Pauli matrix of spin j , respectively, and J_{kl} denotes the scalar coupling between spins k and l .

In the experiment, single-spin z -axis rotations are implemented either through the evolution of the chemical shifts in the Hamiltonian or by RF phase shifts³⁷. Rotations along x - and y -axes are implemented by standard Isech and Hermite-shaped frequency selective RF pulses for spins M and C₁–C₄, and numerically optimized GRAPE pulses^{37,49} for the manipulation of H₁ and H₂ during the pseudo-pure state preparation. Judicious placement of spin-selective refocussing pulses allows us to construct the desired J -coupling evolutions between neighbouring qubits. A custom-built software compiler optimizes the pulse sequences for highest unitary fidelity by minimizing the effects of finite pulsewidth and off-resonance errors as well as unwanted coupling evolutions, using methods that scale polynomially in the number of qubits³⁷. Refocussing pulses are not shown in Fig. 2b,c).

The effects of pulse errors due to RF inhomogeneity over the spin ensemble are reduced by implementing an RF selection technique, that is, a spatial selection of molecules in a region of high RF homogeneity. The linewidth, and therefore the coherence of the ensemble qubits, is also improved^{41,54}. The four carbon spins, initialized in the state **0000**, are used to prepare and measure the CETS, where C₁ is the probe qubit, and C₂–C₄ are the register qubits used to simulate the frustrated magnet. The CETS $|\Psi_\beta\rangle$ is prepared by the pulse sequence shown in Fig. 2b. The NMR signal of C₁ is acquired after the controlled- U_M gate is applied. The controlled- U_M is implemented by combining phase-flip and SWAP gate operations, and is further decomposed into nearest-neighbour coupling evolutions and single spin rotations. As an example, Fig. 2c illustrates the pulse sequence for the observable $Z_1 Z_2 Z_3$.

As indicated in equation (4), $\langle U_M \rangle$ is encoded in the coherent part of the probe qubit (C₁) state. In the spectra of the probe qubit, the coherence is distributed among $2^6 = 64$ resonance peaks, each of which corresponds to a particular eigenstate of the remaining 6 qubits M, H₁, H₂, C₂–C₄. The intensities of these peaks are obtained by a precise spectral fitting procedure⁴⁸.

Since $\sigma^z = 0 - 1$ with $1 \equiv |1\rangle\langle 1|$, the 64 peaks are divided into two antiphase multiplets corresponding to the two eigenstates of H₂. We may, for example, choose the group marked by the H₂ state **0**. By adding the amplitudes of the 8 peaks corresponding to the state **0_M0_{H1}0_{H2}**, $\langle U_M \rangle$ is obtained. As a reference signal to define the phases and magnitudes of the signals acquired to measure $\langle U_M \rangle$, we use the signal of C₁ corresponding to the state **00 σ^z (1+ σ^x)000** obtained by a $\pi/2$ readout pulse applied to C₁ from the initial pseudo-pure state ρ_s (see Fig. 3).

T_1 relaxation of the proton spins. In preparing the CETS and measuring $\langle U_M \rangle$, the proton spins M, H₁ and H₂ ideally remain in the state **00 σ^z** . We measured the decay of the state **00 σ^z 1111** to estimate the effect of the protons' T_1 relaxation process on the measurement of the CETS. The state **00 σ^z 1111** is prepared from ρ_s through phase cycling. After a variable delay, a $\pi/2$ readout pulse for H₂ is applied. The intensity of the signal against the delay time is shown in Supplementary Fig. S3, with a fit yielding a relaxation time of 2.9 s. This relaxation was included along with the carbon T_2 decays in the numerical simulations of the NMR experiment.

T_1 relaxation of the carbon spins. Considering the durations of the experiments listed in Supplementary Table S1 in Supplementary Information, the T_1 relaxation of the carbon spins may explain the asymmetry of fidelity, with respect to the sign of h in Figs 3a–d, in the main text. In principle, the T_1 relaxation could affect the CETS states differently. We take states of the register qubits **|000⟩** and **|111⟩** as examples, where the qubit ordering is C₂–C₃. In the experiments, RF selection was used to improve the fidelity of pulses. The pulse sequence of the RF selection effectively operates as a π pulse to spin M in the initial state ρ^z **1111111**, the state

from which the labelled pseudo-pure state ρ_s was prepared. Hence, the starting point of the experiments is the pseudo-pure state $-\rho_s$. The state of the register qubits **|000⟩** corresponds to a deviation density matrix in the NMR experiment $\rho_{000} = -(\sigma_1^z + \sigma_2^z + \sigma_3^z + \sigma_1^z \sigma_2^z + \sigma_1^z \sigma_3^z + \sigma_2^z \sigma_3^z + \sigma_1^z \sigma_2^z \sigma_3^z)$, and **|111⟩** corresponds to $\rho_{111} = -(-\sigma_1^z - \sigma_2^z - \sigma_3^z + \sigma_1^z \sigma_2^z + \sigma_2^z \sigma_3^z + \sigma_1^z \sigma_3^z - \sigma_1^z \sigma_2^z \sigma_3^z)$. Although we have not checked by explicit simulations or experiments, it is reasonable to speculate that ρ_{000} decays faster than ρ_{111} .

References

- Kohn, W. Nobel lecture: electronic structure of matter-wave functions and density functionals. *Rev. Mod. Phys.* **71**, 1253–1266 (1999).
- Feynman, R. P. Simulating physics with computers. *Int. J. Theor. Phys.* **21**, 467–488 (1982).
- Peng, X., Du, J. & Suter, D. Quantum phase transition of ground-state entanglement in a Heisenberg spin chain simulated in an NMR quantum computer. *Phys. Rev. A* **71**, 012307 (2005).
- Friedenauer, A. *et al.* Simulating a quantum magnet with trapped ions. *Nat. Phys.* **4**, 757–761 (2008).
- Kim, K. *et al.* Quantum simulation of frustrated Ising spins with trapped ions. *Nature* **465**, 590–593 (2010).
- Edwards, E. *et al.* Quantum simulation and phase diagram of the transverse-field Ising model with three atomic spins. *Phys. Rev. B* **82**, 060412 (2010).
- Ma, X.-S. *et al.* Quantum simulation of the wavefunction to probe frustrated Heisenberg spin systems. *Nature Phys.* **7**, 1–7 (2011).
- Lanyon, B. P. *et al.* Towards quantum chemistry on a quantum computer. *Nat. Chem.* **2**, 106–111 (2010).
- Gerritsma, R. *et al.* Quantum simulation of the Dirac equation. *Nature* **463**, 68–71 (2010).
- Weimer, H., Müller, M., Lesanovsky, I., Zoller, P. & Büchler, H. P. A Rydberg quantum simulator. *Nat. Phys.* **6**, 382–388 (2010).
- Barreiro, J. T. *et al.* An open-system quantum simulator with trapped ions. *Nature* **470**, 486–491 (2011).
- Struck, J. *et al.* Quantum simulation of frustrated classical magnetism in triangular optical lattices. *Science* **333**, 996–999 (2011).
- Li, Z. *et al.* Solving quantum ground-state problems with nuclear magnetic resonance. *Sci. Rep.* **1**, 88 (2011).
- Lanyon, B. P. *et al.* Universal digital quantum simulation with trapped ions. *Science* **334**, 57–61 (2011).
- Buluta, I. & Nori, F. Quantum simulators. *Science* **326**, 108–111 (2009).
- Ladd, T. D. *et al.* Quantum computers. *Nature* **464**, 45–53 (2010).
- Kaye, P., Laflamme, R. & Mosca, M. *An Introduction to Quantum Computing* (Oxford University Press, 2007).
- Kassal, I. *et al.* Simulating chemistry using quantum computers. *Annu. Rev. Phys. Chem.* **62**, 185–207 (2011).
- Mezard, M., Parisi, G. & Virasoro, M. A. *Spin Glass Theory and Beyond* (World Scientific, 1987).
- Mattis, D. C. & Swendsen, R. H. *Statistical Mechanics Made Simple*, 2nd edn (World Scientific, 2008).
- Young, A. P., Knysh, S. & Smelyanskiy, V. N. Size dependence of the minimum excitation gap in the quantum adiabatic algorithm. *Phys. Rev. Lett.* **101**, 170503 (2008).
- Nishimori, H. & Wong, K. Statistical mechanics of image restoration and error-correcting codes. *Phys. Rev. E* **60**, 132–144 (1999).
- Istrail, S. Statistical mechanics, three-dimensionality and NP-completeness: I. Universality of intracatability for the partition function of the Ising model across non-planar surfaces. *Proceedings of the Thirty-Second Annual ACM Symposium on Theory of computing* 87–96 (2000).
- Farhi, E. *et al.* A quantum adiabatic evolution algorithm applied to random instances of an NP-complete problem. *Science* **292**, 472–475 (2001).
- Clay Mathematics institute. http://www.claymath.org/millennium/P_vs_NP/ (2012).
- Altshuler, B., Krovi, H. & Roland, J. Anderson localization makes adiabatic quantum optimization fail. *Proc. Natl Acad. Sci. USA* **107**, 12446–12450 (2010).
- Dickson, N. & Amin, M. Does Adiabatic Quantum Optimization Fail for NP-Complete Problems? *Phys. Rev. Lett.* **106**, 050502 (2011).
- De las Cuevas, G., Dür, W., Van den Nest, M. & Martin-Delgado, M. A. Quantum algorithms for classical lattice models. *New J. Phys.* **13**, 093021 (2011).
- Metropolis, N., Rosenbluth, A. W., Rosenbluth, M. N., Teller, A. H. & Teller, E. Equation of state calculations by fast computing machines. *J. Chem. Phys.* **21**, 1087–1092 (1953).
- Robert, C. P. & Casella, G. *Monte Carlo Statistical Methods*, 2nd edn (Springer-Verlag, 2004).
- Temme, K. *et al.* Quantum Metropolis sampling. *Nature* **471**, 87–90 (2011).
- Yung, M.-H. & Aspuru-Guzik, A. A quantum-quantum Metropolis algorithm. *Proc. Natl Acad. Sci. USA* **109**, 754–759 (2012).
- Aldous, D. J. Some inequalities for reversible markov chains. *J. Lond. Math. Soc.* **s2-25**, 564–576 (1982).

34. Lidar, D. & Biham, O. Simulating Ising spin glasses on a quantum computer. *Phys. Rev. E* **56**, 3661–3681 (1997).
35. Yung, M.-H. *et al.* Simulation of classical thermal states on a quantum computer: a transfer-matrix approach. *Phys. Rev. A* **82**, 060302 (2010).
36. Vandersypen, L. M. K. & Chuang, I. L. NMR techniques for quantum control and computation. *Rev. Mod. Phys.* **76**, 1037–1069 (2004).
37. Ryan, C. A. *et al.* Liquid-state nuclear magnetic resonance as a testbed for developing quantum control methods. *Phys. Rev. A* **78**, 012328 (2008).
38. Morgan, J. P., Stein, A., Langridge, S. & Marrows, C. H. Thermal ground-state ordering and elementary excitations in artificial magnetic square ice. *Nat. Phys.* **7**, 75–79 (2010).
39. Wannier, G. Antiferromagnetism. The Triangular Ising Net. *Phys. Rev.* **79**, 357–364 (1950).
40. Castelnovo, C., Moessner, R. & Sondhi, S. L. Magnetic monopoles in spin ice. *Nature* **451**, 42–45 (2008).
41. Knill, E. *et al.* An algorithmic benchmark for quantum information processing. *Nature* **404**, 368–370 (2000).
42. Winograd, E. A., Rozenberg, M. J. & Chitra, R. Weak-coupling study of decoherence of a qubit in disordered magnetic environments. *Phys. Rev. B* **80**, 214429 (2009).
43. Lloyd, S. Universal quantum simulators. *Science* **273**, 1073–1078 (1996).
44. Leskowitz, G. & Mueller, L. State interrogation in nuclear magnetic resonance quantum-information processing. *Phys. Rev. A* **69**, 052302 (2004).
45. Barenco, A. *et al.* Elementary gates for quantum computation. *Phys. Rev. A* **52**, 3457–3467 (1995).
46. Nielsen, M. A. & Chuang, I. L. *Quantum Computation and Quantum Information* (Cambridge University Press, 2000).
47. Chuang, I. L. *et al.* Bulk quantum computation with nuclear magnetic resonance: theory and experiment. *Proc. R. Soc. Lond. A* **454**, 447–467 (1998).
48. Souza, A. M. *et al.* Experimental magic state distillation for fault-tolerant quantum computing. *Nat. Commun.* **2**, 169 (2011).
49. Khaneja, N. *et al.* Optimal control of coupled spin dynamics: design of NMR pulse sequences by gradient ascent algorithms. *Journal of magnetic resonance. J. Magn. Reson.* **172**, 296–305 (2005).
50. Zhang, J., Grassl, M., Zeng, B. & Laflamme, R. Experimental Implementation of a Codeword Stabilized Quantum Code preprint as arXic:1111.5445.
51. Negrevergne, C. *et al.* Benchmarking quantum control methods on a 12-qubit system. *Phys. Rev. Lett.* **96**, 170501 (2006).
52. Baugh, J. *et al.* Solid-state NMR three-qubit homonuclear system for quantum-information processing: control and characterization. *Phys. Rev. A* **73**, 022305 (2006).
53. Mehring, M. & Mende, J. Spin-bus concept of spin quantum computing. *Phys. Rev. A* **73**, 052303 (2006).
54. Maffei, P., Elbayed, K., Broundeau, J. & Canet, D. Slice selection in NMR imaging by use of the B_1 gradient along the axial direction of a saddle-shaped coil. *J. Magn. Reson.* **95**, 382–386 (1991).

Acknowledgements

We thank M. Gingras and J. D. Whitfield for insightful discussions and comments, and are grateful to the following funding sources: Croucher Foundation (M.H.Y.); DARPA under the Young Faculty Award N66001-09-1-2101-DOD35CAP, the Camille and Henry Dreyfus Foundation, and the Sloan Foundation; Army Research Office under Contract No. W911NF-07-1-0304 (A.A.G.); CIFAR, SHARCNET and QuantumWorks (R.L.), and NSERC (J.F.Z., R.L. and J.B.).

Author contributions

J.-F.Z. and J.B. designed the NMR experiments and simulations, which were carried out by J.-F.Z.; M.-H.Y. and A.A.-G. made the theoretical proposal and contributed to the analysis of results. R.L. and J.B. supervised the experiment. All authors contributed to the writing of the paper and discussed the experimental procedures and results.

Additional information

Supplementary Information accompanies this paper at <http://www.nature.com/naturecommunications>

Competing financial interests: The authors declare no competing financial interests.

Reprints and permission information is available online at <http://npg.nature.com/reprintsandpermissions/>

How to cite this article: Zhang, J. *et al.* Digital quantum simulation of the statistical mechanics of a frustrated magnet. *Nat. Commun.* **3**:880 doi: 10.1038/ncomms1860 (2012).